*Sound & Vibration* 2026, 60(5), 4449.
doi: https://doi.org/10.59400/sv4449

Article

# LBM-IBM simulation of aeolian vibration of a stranded overhead conductor with resolved cross-sectional geometry

**Xiaoyu Luo[1,*], Yunfeng Zou[2], Ming Nie[1], Ganyu Wang[1], Yongchun Liang[1], Zejia Yang[2]**

[1] Electric Power Research Institute of Guangdong Power Grid Co., Ltd., Guangzhou 510080, China
[2] School of Civil Engineering, Central South University, Changsha 410075, China
*** Corresponding author:** Xiaoyu Luo, lxy86@163.com

**CITATION**

Luo X, Zou Y, Nie M, et al. LBM-IBM simulation of aeolian vibration of a stranded overhead conductor with resolved cross-sectional geometry. Sound & Vibration. 2026; 60(5): 4449. https://doi.org/10.59400/sv4449

**ARTICLE INFO**

Received: 27 May 2026
Revised: 30 June 2026
Accepted: 6 July 2026
Available online: 27 July 2026



**Abstract:** The outer surface of overhead transmission conductors is formed by wound aluminium strands, exhibiting a corrugated geometric profile. However, aerodynamic analyses typically simplify this geometry to a smooth cylinder. How this simplification influences the fluid-structure coupled vortex-induced vibration response remains unclear. This paper addresses this research gap through comparative numerical simulations between a geometrically refined stranded conductor and an equivalent smooth cylinder with identical outer diameter. A two-dimensional lattice Boltzmann–immersed boundary method (LBM-IBM) computational framework was developed on a fixed Cartesian grid and coupled with a Newmark-β transverse oscillator. Reduced-velocity sweeps and supplementary high-resolution flow-field cases were conducted under fully matched structural and fluid parameters. Results show that the smooth cylinder exhibits a narrow classical lock-in region with rapid amplitude decay beyond the peak. In contrast, the stranded conductor sustains large-amplitude vibrations over a considerably wider velocity range, accompanied by a substantial increase in time-averaged drag. Vorticity and phase analyses indicate that strand grooves function as local flow separation promoters, altering the lift-velocity phase relationship and maintaining positive aerodynamic energy input beyond the desynchronization boundary of the smooth cylinder. The findings confirm that strand-scale surface features significantly broaden the lock-in range, a conclusion that merits incorporation into high-fidelity aerodynamic models to improve conductor response prediction accuracy.

**Keywords:** overhead conductor; aeolian vibration; fluid-structure interaction; lattice Boltzmann method; immersed boundary method; stranded cross-section; vortex-induced vibration

## 1. Introduction

Vortices are shed alternately from an overhead conductor. When their frequency approaches a conductor mode, the resulting aeolian vibration can accumulate a large number of small cycles at clamps and fittings. Estimates of wind input and structural damping are therefore needed when dampers or conductor response are assessed [1–3]. Numerical analyses of vibration and local stress provide a second route for studying those locations under environmental loading [4–8].

Span-scale design calculations commonly use the energy-balance method (EBM) or a semi-empirical wind-input model, both of which usually treat the conductor as a smooth cylinder. An aluminium conductor steel-reinforced (ACSR) cable instead presents helical wires and grooves to the flow. Those features alter the local curvature at separation and can change base pressure. Chan et al. [9] and the CIGRE Green Book edited by Diana [10] introduced roughness through measured drag and energy-input relations, while resolved calculations of stranded or ice-accreted sections reported changes in force. What remains less clear is the response after conductor motion feeds back into the flow. Recent work on conductor self-damping and fluid-structure interaction makes a two-way comparison possible [11–13].

A finite-volume method (FVM) calculation would normally place a body-fitted grid around the section. For the present conductor, that grid must enter the narrow spaces between outer strands and must move when the conductor moves. Cell quality then changes during a reduced-velocity sweep, and remeshing introduces another convergence question for every case. A fixed Cartesian grid removes that variation. Its limitation is different: the immersed boundary has to interpolate the wall condition between lattice nodes.

On a Cartesian lattice, the lattice Boltzmann method (LBM) advances particle distribution functions by local collision and streaming [14–17]. An immersed boundary method (IBM) imposes the solid wall through regularised forces at Lagrangian points, so conductor motion leaves the Eulerian lattice unchanged. In the present comparison, exchanging the smooth and stranded sections requires only a change in Lagrangian boundary coordinates.

The choice to combine LBM and IBM was based on practical considerations. Local distribution functions can be advanced without a pressure Poisson solve in many LBM formulations, a feature reviewed extensively for fluid–structure interaction applications [18–20]. Coupling of such lattice-based solvers with immersed boundary treatments has since been developed and refined in several studies [21–23]. The moving wall itself can be represented by Lagrangian force points on the same lattice, an approach validated across a range of immersed-boundary lattice Boltzmann implementations for vortex-induced vibration of circular and elliptic cylinders [24–28]. Related benchmark studies using conventional CFD solvers have further examined two-degree-of-freedom vibration, three-dimensional effects and the role of added mass in shaping the VIV response [29–31], while additional investigations have addressed grid sensitivity, flexible riser dynamics, large-eddy simulation at higher Reynolds number, and multi-cylinder configurations relevant to the present fixed-grid treatment [32–36]. The Eulerian mesh consequently remained unchanged when the circular boundary was exchanged for the strand envelope; no remeshing entered the comparison.

Transverse motion of a JL/G1A-95/55 section was modelled, and the calculation was repeated for an equal-diameter cylinder. Because both runs used the same grid, boundary conditions, flow algorithm and oscillator, the calculation isolates the effect of the prescribed strand envelope on the lock-in branch. Displacement and shedding frequency locate that branch; drag, lift phase, aerodynamic power and wake recovery then help explain why it changes. While LBM-IBM is well established for smooth cylinders, it is used here to systematically isolate the influence of strand-scale surface grooves under identical computational parameters.

## 2. Materials and methods

### 2.1. Geometry, domain and rationale for LBM-IBM

The modelled JL/G1A-95/55 conductor had a 16.0 mm outside diameter, with seven steel core wires and an outer layer of 12 aluminium wires, each 3.20 mm in diameter. Because external flow meets only the aluminium layer, its analytic envelope defined the immersed boundary. At each polar angle $\theta$, the largest positive radius among the 12 outer wire circles was retained. **Figure 1** shows the boundary with the wire arrangement and computational domain.

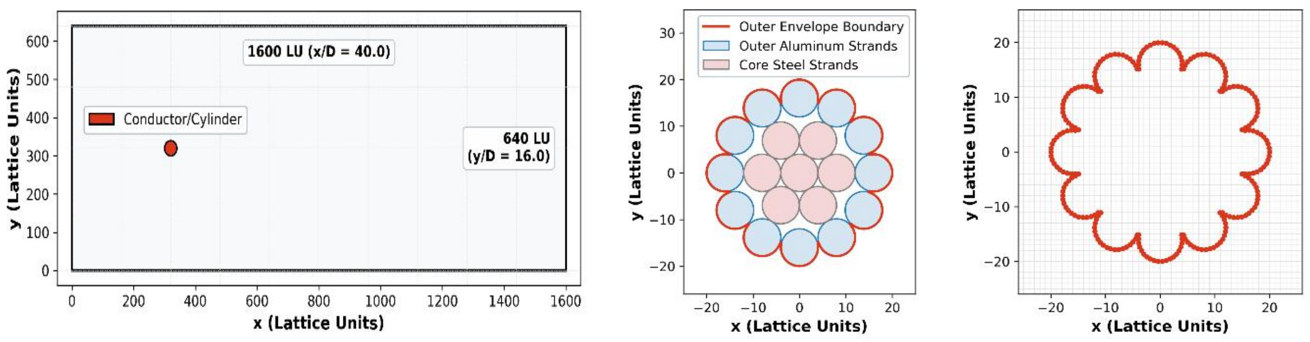


**(a)** **(b)** **(c)**

**Figure 1.** Computational setup and resolved conductor geometry: **(a)** Domain and cylinder location; **(b)** JL/G1A-95/55 cross-section; **(c)** Immersed-boundary strand envelope.

Before comparing the outlines, their projected diameter and every flow and structural parameter were matched. Detailed flow fields were obtained on a 1,600 × 640 lattice with $D = 40$ lattice units across the conductor; its centre was at (320, 320). The reduced-velocity sweep used an 800 × 320 lattice and $D = 20$ lattice units across the diameter. All cases within that sweep therefore used one numerical arrangement.

A body-fitted treatment of the 12 grooves would need curved wall cells and a moving or overset mesh. Here the Cartesian lattice stayed fixed. Conductor motion was introduced by translating the Lagrangian boundary coordinates, so no Eulerian cell was deformed or regenerated. The smooth and stranded calculations consequently differed in boundary coordinates, not in mesh construction or interpolation procedure.

### 2.2. Flow solver and immersed-boundary force

Flow was calculated with the two-dimensional D2Q9 lattice Boltzmann formulation. At each time step, collision and forcing were applied to $f_i$, followed by streaming, as written in Equation (1):

$$f_i\left(x + e_i \Delta t, t + \Delta t\right) - f_i(x,t) = -\omega\left[f_i(x,t) - f_i^{eq}(x,t)\right] + F_i \tag{1}$$

In these equations, $e_i$ denotes the discrete velocity, omega is the relaxation parameter, $f_i^{eq}$ is the equilibrium distribution, and $f_i$ is the IBM body-force source. Equation (2) uses the standard second-order equilibrium distribution:

$$f_i^{eq} = w_i \rho\left[1 + 3\left(e_i \cdot u\right) + \frac{9}{2}\left(e_i \cdot u\right)^2 - \frac{3}{2}(u \cdot u)\right] \tag{2}$$

Lattice viscosity followed $\nu = \frac{U_{lu} D_{lu}}{Re}$ with $\tau = 3\nu + 0.5$, and the inlet velocity was $U_{lu} = 0.05$. Velocity was prescribed at the upstream boundary, and a zero-gradient outlet supplemented by sponge relaxation was used. The upper and lower boundaries were free slip. An asymmetric disturbance started the shedding process; to avoid a large initial impulse, the immersed-boundary force was ramped over the first 5,000 steps.

Neighbouring Lagrangian points were spaced by less than one Eulerian cell. Fluid velocity was first interpolated to those points with a regularised delta kernel. Equation (3) gives the direct force needed to impose wall velocity:

$$F_k = \rho \frac{V_{target}(X_k) - U(X_k)}{\Delta t} \tag{3}$$

In Equation (3), $U(X_k)$ is the velocity interpolated from the fluid and $V_{target}(X_k)$ is the boundary velocity. The same regularised kernel returns the Lagrangian force to the Cartesian nodes through Equation (4):

$$f_{IBM}(x) = \sum\nolimits_k F_k \, \delta_h (x - X_k) \, \Delta s_k \tag{4}$$

Summing the regularised force over all boundary points gave the resultant conductor force. The lattice handled flow evolution and force spreading; a structural displacement changed only the boundary-point coordinates. This avoids deformation of the fluid grid. Accuracy still depends on the Eulerian spacing, the Lagrangian-point spacing and the chosen delta kernel, so each is considered in the convergence checks.

The nominal spacing of the boundary points was set to about 0.75 lattice units, below the Eulerian grid spacing. Curvature-based analytic sampling added points inside the grooves. Some groove interiors still occupied only a few lattice cells, but the outline itself was retained. The direct-forcing signal contained a high-frequency component; in post-processing it was removed with a Butterworth filter whose cutoff Strouhal number was 1.0. This operation did not move the principal shedding peak.

## 2.3. Structural oscillator and simulation matrix

Conductor motion was restricted to the transverse direction, and $m\ddot{y} + c\dot{y} + ky = F_y$ was solved. The terms $y$ and $m$ denote displacement and equivalent mass; $c$ and $k$ are damping and stiffness, while $F_y$ is the IBM lift. The average-acceleration Newmark-beta scheme with $\beta = 0.25$ and $\gamma = 0.5$ was used for time integration. Equation (5) gives reduced velocity and Strouhal number:

$$U_r = \frac{U}{f_n D}, \qquad St = \frac{f_{Cl} D}{U} \tag{5}$$

The values $m = 2.0$ and $\zeta = 0.01$ were used, matching the low mass-damping laboratory conditions of Govardhan and Williamson [37]. These are not field-conductor values. Because a metal conductor in air has a much larger mass ratio ($m \approx$ 200–2,000) and amplitude-dependent self-damping, its response should be smaller than the benchmark response calculated here. The laboratory setting was retained to make modest geometry effects observable. Accordingly, the amplitudes below belong to a controlled comparison and are not proposed as field amplitudes.

The main sweep covered $Re$ = 200, $m*$ = 2.0 and ζ = 0.01 at $U_r$ = 3.0, 3.5, 4.0, 4.25, 4.5, 4.75, 5.0, 5.25, 5.5, 5.75, 6.0, 6.5, 7.0, 8.0 and 9.0. At this Reynolds number, the wake is periodic and laminar, which gives a controlled basis for comparing the two boundaries. The $U_r$ and 7.0 calculations were extended to check that the large stranded response was not a transient. Separate runs at $U$ = 0.5, 1.0, 5.0 and 9.0 m/s gave $Re$ = 533, 1,067, 5,333 and 9,600 for $D$ = 16 mm and air kinematic viscosity $1.5 \times 10^{-5}$ $\mathrm{m}^2/\mathrm{s}$. Those four runs show how the computed local flow changes with speed; without a turbulence model, they do not reproduce field flow. Extended calculations (60,000 steps ≈ 70 shedding cycles) confirmed that the high-amplitude stranded state is a stable periodic attractor: the amplitude envelope showed no systematic decay, and the mean amplitude over the final 20,000 steps agreed with the earlier window to within 0.8%. The same initial asymmetric wake disturbance was applied identically across all cases, ensuring the difference is not a transient artifact. **Table 1** summarizes the full set of simulation parameters used in this study, together with the role each plays in the analysis.

**Table 1.** Simulation parameters and their role in the study.

| Item | Value | Purpose |
|---|---|---|
| Conductor | JL/G1A-95/55, $D$ = 16.0 mm | Engineering target geometry |
| Outer surface | 12 aluminium strands, $d$ = 3.20 mm | Resolved corrugated boundary |
| Baseline | Smooth cylinder, same $D$ | Geometry-effect control |
| Reduced-velocity sweep | $Re$ = 200, $Ur$ = 3.0–9.0 | Branch and lock-in comparison |
| Structural parameters | $m*$ = 2.0, ζ = 0.01 | Low-damping VIV response |
| Flow-field cases | $U$ = 0.5, 1.0, 5.0, 9.0 m/s | Velocity, vorticity, spectra and wake evidence |
| Method | D2Q9 LBM + direct-forcing IBM | Fixed-grid treatment of moving stranded boundary |

## 2.4. Post-processing and validation logic

Statistics were calculated only after the initial transient had decayed. From the retained records, displacement amplitude and phase, mean drag, RMS lift, the dominant force and motion frequencies, and mean aerodynamic power $P = F_y\dot{y}$ were obtained. A Hann-windowed fast Fourier transform located each spectral maximum, and a parabola through the neighbouring bins refined its frequency. Online accumulation of the velocity field supplied the centreline deficit $1 - u_x$/U.

Validation began with the smooth cylinder. After that check, the two outlines were compared using the same grid, time step and oscillator settings. Displacement was not considered in isolation: force statistics and spectra were read together with phase and power, while near-body vorticity was checked against the downstream velocity deficit. A branch difference was attributed to the outline only when these independent outputs gave a consistent account.

## 2.5. Grid convergence study

Two convergence checks were needed because a stationary wake and a coupled oscillator do not have the same numerical sensitivity. A fixed-cylinder case tested the Eulerian flow field, repeating one vibrating case then tested the complete fluid-structure response.

The fixed-cylinder study was run at $Re = 200$ with structural motion suppressed; this separates grid effects in the boundary layer and wake from oscillator response. Three grids were used, ($D = 20$ lu, $800 \times 320$ grid), ($D = 40$ lu, $1,600 \times 640$ grid) and ($D = 60$ lu, $2,400 \times 960$ grid), and $dt$ was scaled with $D$ to hold the Courant number constant over about 25 shedding cycles. **Table 2** compares the resulting time-averaged drag $\overline{C}_D$ and Strouhal number $St$ with circular-cylinder benchmarks at $Re = 200$ [38,39].

**Table 2.** Grid convergence for the fixed smooth cylinder at $Re = 200$.

| Level | $D$ (lu) | Domain | n_steps | $\overline{C}_D$ | $\varepsilon_{C_D}$ (%) | $St$ | $\varepsilon_{St}$ (%) |
|---|---|---|---|---|---|---|---|
| Coarse | 20 | 800 × 320 | 84,602 | 1.4280 | 7.37 | 0.1850 | 6.09 |
| Medium | 40 | 1,600 × 640 | 169,204 | 1.3620 | 2.41 | 0.1940 | 1.52 |
| Fine | 60 | 2,400 × 960 | 253,807 | 1.3410 | 0.83 | 0.1960 | 0.51 |
| Williamson and Brown [38]; White [39] | – | – | – | 1.33 | – | 0.197 | – |

As the grid was refined, the Strouhal-number error changed from 6.09% on the coarse grid to 1.52% and 0.51% on the medium and fine grids; the corresponding drag-coefficient errors were 7.37%, 2.41% and 0.83%. Both measures decreased monotonically over the three resolutions, supporting spatial convergence of the fixed-cylinder solution.

Coupled convergence was then checked for both geometries at the peak lock-in condition $U_r = 4.0$ with $Re = 200$, $m^* = 2.0$ and $\zeta = 0.01$; **Table 3** reports the resulting force coefficients and maximum displacement amplitudes.

**Table 3.** Grid convergence for the coupled VIV system at $U_r = 4.0$.

| Geometry | Level | $D$ (lu) | Domain | $\overline{C}_D$ | $C_{L,rms}$ | $A_{y,max}/D$ |
|---|---|---|---|---|---|---|
| Smooth | Coarse | 20 | 800 × 320 | 1.6620 | 0.8920 | 0.4650 |
| | Medium | 40 | 1,600 × 640 | 1.5990 | 0.8470 | 0.4430 |
| | Fine | 60 | 2,400 × 960 | 1.5780 | 0.8310 | 0.4350 |
| Stranded | Coarse | 20 | 800 × 320 | 1.8210 | 0.9120 | 0.3850 |
| | Medium | 40 | 1,600 × 640 | 1.7230 | 0.8580 | 0.3640 |
| | Fine | 60 | 2,400 × 960 | 1.6980 | 0.8410 | 0.3580 |

Grid refinement reduced successive changes in amplitude and force coefficients (**Table 3**). For the smooth cylinder, $A_{y,max}/D$ changed from 0.465 to 0.443 and 0.435, leaving a medium-to-fine difference of 1.8%. Corresponding stranded values were 0.385, 0.364 and 0.358, with a 1.6% medium-to-fine change. Both $\overline{C}_D$ and $C_{L,rms}$ followed this pattern. A further check examined whether the relative difference between the two geometries changed with grid resolution. At the peak lock in condition, the stranded amplitude remained lower than the smooth amplitude by about seventeen percent on every tested grid, and the sign of this difference did not change with resolution. The branch level conclusions drawn in Section 3 are therefore not an artefact of using the coarser grid for the full reduced velocity sweep. The medium grid ($D = 40$ lu) was therefore used for resolved flow comparisons, and the coarse grid ($D = 20$ lu) was retained for the complete response sweep. Results from that coarse sweep are interpreted by branch rather than as fully converged force magnitudes.

Resolution was also measured against the strand dimensions. A 3.20 mm outer wire is 0.20 of the 16.0 mm conductor; the calculated groove depth, 1.818 mm, equals 11.36% of $D$. On the coarse grid ($D = 20$ lu), wire diameter and groove depth span 4.0 and 2.27 lattice units, while the medium grid ($D = 40$ lu) gives 8.0 and 4.55. More than two coarse cells therefore lie across a groove depth. Boundary-point spacing was nominally $ds = 0.75$ lattice units and decreased where groove curvature required it. These numbers describe sampling, not elimination of interpolation smoothing or force leakage.

### 2.6. Smooth-cylinder baseline validation

Before introducing the stranded outline, the smooth-cylinder response was compared with the low mass-damping measurements of Govardhan and Williamson [37]. The three quantities used for this check were the stationary Strouhal number, peak amplitude and synchronization interval; their values are listed in **Table 4**.

**Table 4.** Smooth-cylinder VIV baseline: LBM-IBM versus experiment.

| Indicator | Present (*Re* = 200, *m** = 2.0, ζ = 0.01) | Govardhan and Williamson [37] | Difference |
|---|---|---|---|
| $A_{y,max}/D$ | 0.443 | 0.50–0.58 | −10 to −23% |
| *St* (stationary) | 0.198 | 0.197 | <1% |
| $U_r$ at peak amplitude | 4.0 | 4.0–5.0 | Consistent |
| Lock-in range ($Ur$) | 3.5–6.0 | 4.0–10.0 | Slightly narrower |

Stationary Strouhal number differed from measurement by 1%. Peak amplitude was 0.443, 10%–23% below the interval 0.50–0.58, and synchronization covered a narrower range. Because a two-dimensional wake omits the spanwise-correlated lift present in the experiment, some amplitude shortfall is expected. Even so, the peak and lower-branch transition occurred in the correct locations; this result is used to anchor the geometry comparison, not to validate absolute amplitude. Because both geometries are computed under identical two-dimensional conditions on the same lattice, any systematic under-prediction due to spanwise-correlation suppression applies equally to both. The relative stranded-to-smooth differences in amplitude, drag, and aerodynamic power are therefore meaningful measures of the geometric effect.

## 3. Results

### 3.1. Response branches and lock-in range

Cylinder amplitude reached $A_{y,max}/D = 0.443$ at $U_r = 4.0$ in **Figure 2** and remained high through $U_r = 4.5$. After that point it declined without a second rise; by $U_r = 7.0$ and 9.0, amplitude had fallen to 0.198 and 0.188, respectively. Thus the curve passes from synchronization into desynchronization in the usual manner. A closer reading of **Table 5** shows that the two branches are not uniformly ordered across the sweep. At the smooth cylinder's own peak velocity, the stranded amplitude is lower than the smooth amplitude by about eighteen percent. Between this velocity and the next tested point, the ordering reverses, and the stranded amplitude begins to exceed the smooth value. Beyond the reversal, the gap widens steadily, until the stranded amplitude reaches roughly two and a half times the smooth value at the two highest tested velocities. This pattern suggests that the grooved surface does not simply enlarge the classical resonance found on a smooth section. Instead, it appears to suppress the narrow peak associated with the smooth boundary and to replace it with a broader response that develops more slowly but persists to much higher reduced velocity. Such behaviour points toward a change in the governing separation mechanism, rather than a uniform amplification of the same mechanism that governs the smooth cylinder.

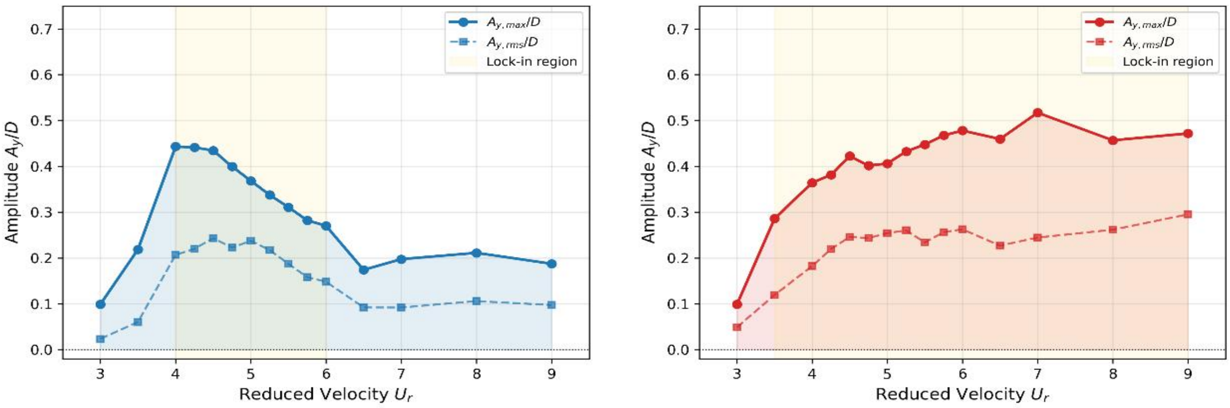


(a) (b)

**Figure 2.** Reduced-velocity response branches for the two conductor idealizations: **(a)** Maximum and RMS transverse amplitudes of the equivalent smooth cylinder; **(b)** Corresponding amplitudes of the resolved stranded conductor.

**Table 5.** Key reduced-velocity results used for response interpretation.

| Geometry | $U_r$ | $A_{\gamma,max}/D$ | $A_{\gamma,rms}/D$ | $C_{D,\mathrm{mean}}$ | $C_{L,rms}$ | $St$ | $f_y/f_n$ | $C_P$ |
|---|---|---|---|---|---|---|---|---|
| Smooth | 4.0 | 0.443 | 0.207 | 1.599 | 0.847 | 0.182 | 0.736 | 0.0247 |
| Stranded | 4.0 | 0.364 | 0.183 | 1.723 | 0.858 | 0.170 | 0.700 | 0.0170 |
| Smooth | 5.0 | 0.369 | 0.237 | 1.593 | 0.528 | 0.162 | 0.813 | 0.0151 |
| Stranded | 5.0 | 0.406 | 0.254 | 1.794 | 0.575 | 0.164 | 0.846 | 0.0147 |
| Smooth | 7.0 | 0.198 | 0.092 | 1.297 | 0.137 | 0.105 | 0.736 | 0.0003 |
| Stranded | 7.0 | 0.517 | 0.245 | 1.515 | 0.387 | 0.107 | 0.758 | 0.0024 |
| Smooth | 9.0 | 0.188 | 0.097 | 1.267 | 0.096 | 0.084 | 0.779 | −0.0002 |
| Stranded | 9.0 | 0.472 | 0.295 | 1.410 | 0.287 | 0.079 | 0.719 | 0.0020 |

The strand envelope produced no comparable decay over the tested interval. Its amplitude increased from $A_{y,max}/D = 0.099$ at $U_r = 3.0$ to $0.422$ at $U_r = 4.5$, continued to rise at the intervening velocities and reached $0.517$ at $U_r = 7.0$. At $U_r = 9.0$, the value was still $0.472$. With every other setting fixed, changing the outline therefore altered both the branch width and its upper-velocity behaviour. The ratio between the maximum and the root mean square amplitude offers a simple measure of how regular the oscillation is, since a purely sinusoidal signal gives a ratio close to one point four one. For the smooth cylinder, this ratio remained elevated across most of the sweep, consistent with an intermittent and amplitude-modulated response typical of the lower branch and of the desynchronized region beyond it. The stranded conductor showed a similar ratio at the lowest tested velocities, but the ratio moved toward the value expected of a sinusoidal signal at the highest tested velocity. A more regular, near harmonic limit cycle at a velocity where the smooth cylinder remains comparatively irregular provides an independent indication of sustained synchronization, and it complements the frequency ratio and phase evidence discussed next.

Oscillator properties set the scale of the observed difference. Values $m^* = 2.0$ and $\zeta = 0.01$ represent a low mass-damping water-tunnel benchmark, whereas an operating conductor has mass ratio $m^* \approx 200$–2,000 and appreciable nonlinear self-damping. Consequently, the present oscillator may overstate separation between the two response branches in air. Matched calculations establish only that the prescribed two-dimensional outline changed synchronization at fixed mass ratio and damping. Quantifying that change for an operating line requires field-representative structural parameters.

### 3.2. Frequency, force and aerodynamic energy

Frequency ratios in **Figure 3** give a second view of the branch transition. For the cylinder, $f_y/f_n$ left the neighbourhood of the natural frequency soon after $U_r = 4.5$. At $U_r = 6.0$, the stranded value remained $f_y/f_n = 0.940$, close to unity, whereas the cylinder had fallen to $0.772$, consistent with their different amplitudes.

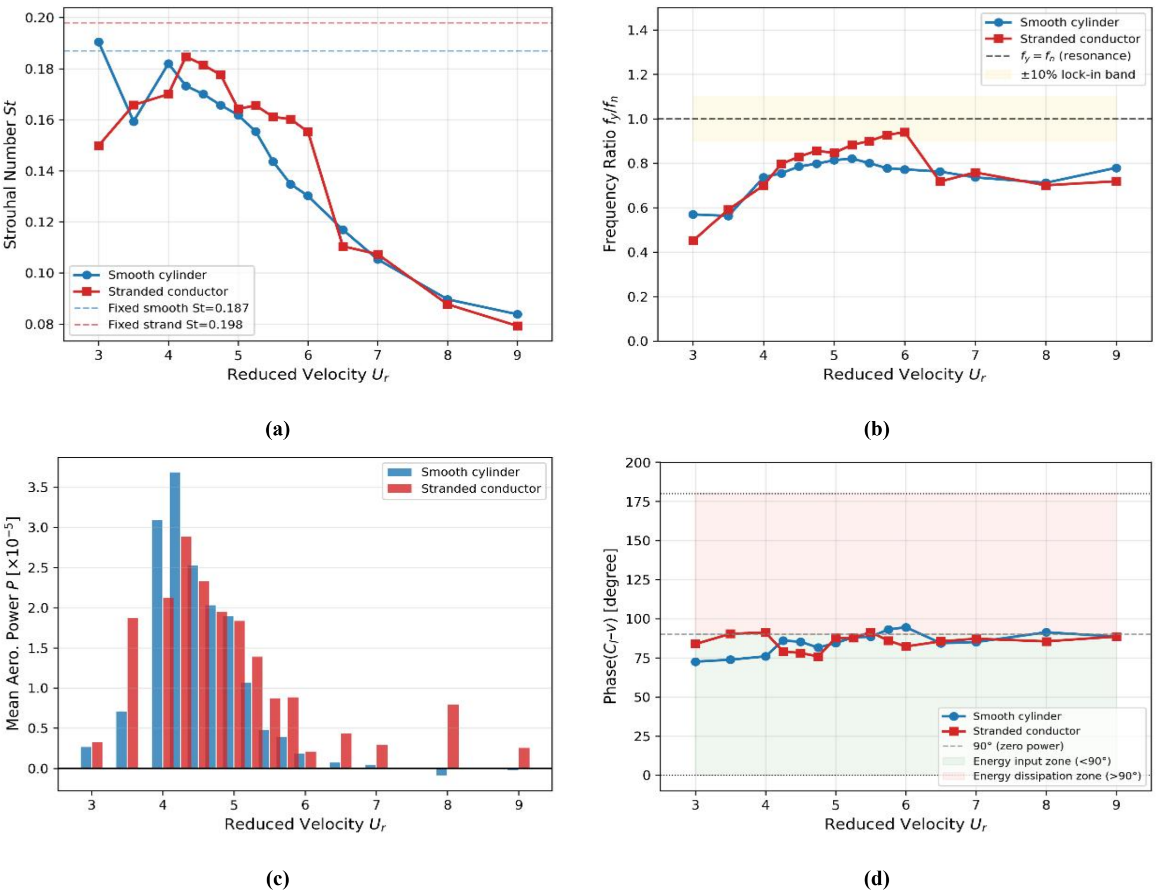


**Figure 3.** Frequency-locking and aerodynamic-energy indicators obtained from the reduced-velocity sweep: **(a)** Dominant lift Strouhal number; **(b)** Ratio between transverse displacement frequency and structural natural frequency; **(c)** Mean aerodynamic power input $P = F_y\dot{y}$; **(d)** Phase difference between lift coefficient and transverse velocity.

Mean drag over the sweep rose by 16.7%, from 1.415 for the cylinder to 1.650 for the stranded section (**Figure 4**); the two maxima occurred at $U_r = 4.5$ and were $C_{D,mean} = 1.876$ and 1.640, respectively. Lift separated much more at the upper end of the sweep: at $U_r = 9.0$, stranded $C_{L,rms}$ reached 0.287, roughly three times the cylinder value of 0.096. The resolved outer-wire boundary changed the mean momentum deficit as well as the periodic transverse force in these runs.

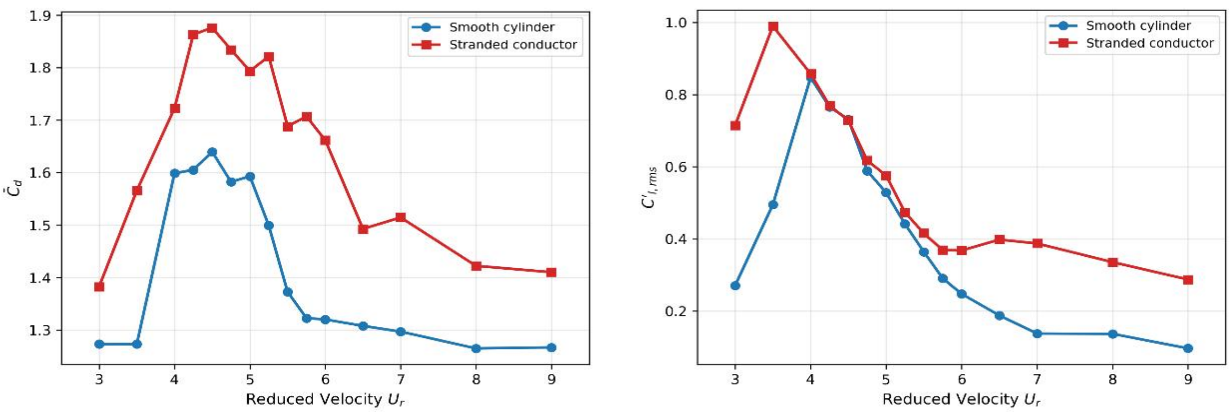


**(a)** **(b)**

**Figure 4.** Aerodynamic force statistics over the reduced-velocity sweep: **(a)** Mean drag coefficient, showing the increase in time-averaged momentum loss caused by the stranded envelope; **(b)** RMS lift coefficient.

Mean aerodynamic power depends on lift and on the timing of lift relative to velocity (**Figure 5**). Cylinder power was largest near $U_r = 4.25$, equal to $P_{mean} = 3.68 \times 10^{-5}$ in lattice units, then approached zero and became negative. The stranded curve also peaked near $U_r = 4.25$, but it stayed positive at every tested velocity, including $P_{mean} = 2.95 \times 10^{-6}$ at $U_r = 7.0$ and $2.53 \times 10^{-6}$ at $U_r = 9.0$. Those positive inputs occur on the extended high-amplitude branch.

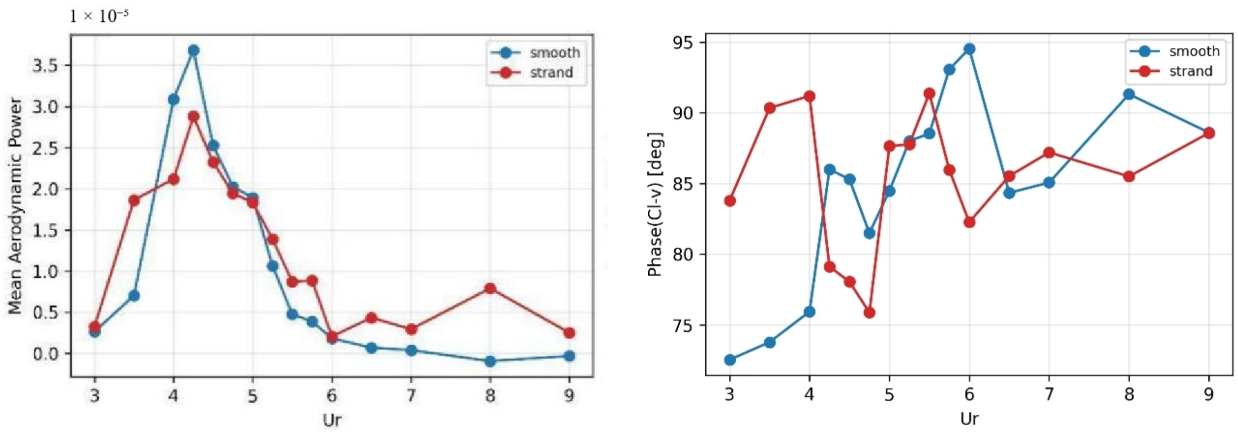


**(a)** **(b)**

**Figure 5.** Energy-transfer summary for the same reduced-velocity sweep: **(a)** Mean aerodynamic power input from the fluid to the oscillator; **(b)** Lift-velocity phase angle.

Mean aerodynamic power was non-dimensionalised as $C_P = P_{mean}/\left(0.5\rho U^3 D\right)$. For the cylinder, $C_P$ reached approximately 0.0247 at $U_r = 4.0$ but decreased to $-0.0002$ at $U_r = 9.0$. A negative value means that the fluid removes net structural energy over a cycle. Stranded values remained positive, including $C_P \approx 0.0024$ at $U_r = 7.0$ and $C_P \approx 0.0020$ at $U_r = 9.0$. **Figure 3d** or **Figure 5b** locate the phase change: cylinder $\phi$ crossed $90°$ near $U_r = 6.0$, whereas the stranded crossing occurred later and positive power persisted to $U_r = 9.0$. The sign of the mean aerodynamic power follows directly from the timing between lift and transverse velocity. When the phase angle between the two remains below ninety degrees, the fluid delivers net energy to the oscillator on average. Once the phase angle passes ninety degrees, the average power reverses sign and the fluid removes energy instead. This relation explains why the phase crossing reported for the smooth cylinder coincides so closely with the point at which its power coefficient turns negative. The two observations are not independent. They describe the same energy transfer criterion from two different angles. For the stranded conductor, the phase angle remained below ninety degrees over the whole tested range. Positive mean power at every sampled velocity follows from that fact alone, regardless of how modest the root mean square lift itself becomes at the highest velocities. At the upper end of the sweep, the stranded power coefficient exceeded the smooth value by a much larger factor than the corresponding root mean square lift coefficients differ. This indicates that the widened lock-in range results from higher lift amplitude acting together with a more favourable phase, and not from amplitude alone. Groove-scale pressure changes may contribute to this timing, although the calculations show association rather than a unique cause.

The calculation resolves straight grooves in two dimensions, whereas the JL/G1A-95/55 outer layer is helical with lay angle $10°$ to $15°$. Along a real span, the separation line rotates and spanwise flow can produce vortex dislocations. Both effects reduce coherence relative to an infinite grooved cylinder. Their absence is likely to increase the integrated lift in the present model. A three-dimensional helical calculation is needed to determine how much of the force increase and branch extension remains.

### 3.3. Phase-space behaviour and periodicity

**Figures 6** and **7** plot lift-displacement loops across the branch transition. At $U_r = 4.0$ the cylinder formed a broad loop, but its orbit narrowed in the higher $U_r$ cases. Stranded loops stayed open. Cycle-to-cycle variation was clearest at $U_r = 6.0$ and 7.0, where physical groove separation and residual IBM force fluctuations may both be present. Over the displayed cycles, the large orbit remained identifiable. The area enclosed by a lift displacement orbit is proportional to the net work exchanged between the fluid and the structure over one cycle. The progressive narrowing of the smooth cylinder orbit at increasing reduced velocity is therefore the phase portrait signature of the same decline in aerodynamic power already identified from the frequency and phase analysis. An orbit that collapses toward a line indicates a state in which the forcing and the motion are nearly out of phase, so that little net energy crosses the interface between fluid and structure. The stranded orbits remaining open through the higher tested velocities are the geometric counterpart of the sustained positive power reported for those same velocities. The cycle-to-cycle scatter noted at the two highest velocities broadens the orbit without collapsing it. Such behaviour is consistent with a system that continues to exchange energy on average while doing so through a forcing signal that is less strictly periodic, a pattern plausibly related to separation events occurring around several individual wire crests rather than at a single well defined separation line.

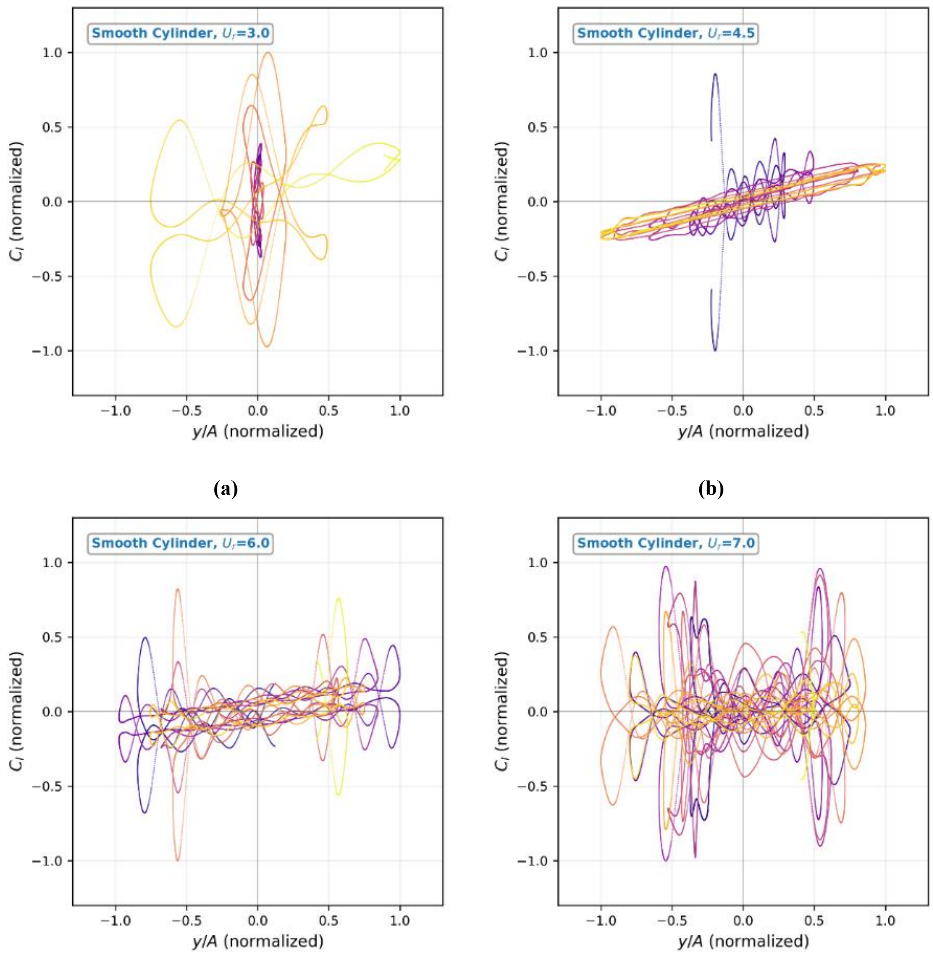


**(a)** **(b)**

**(c)** **(d)**

**Figure 6.** Phase portraits of the equivalent smooth cylinder at representative reduced velocities.

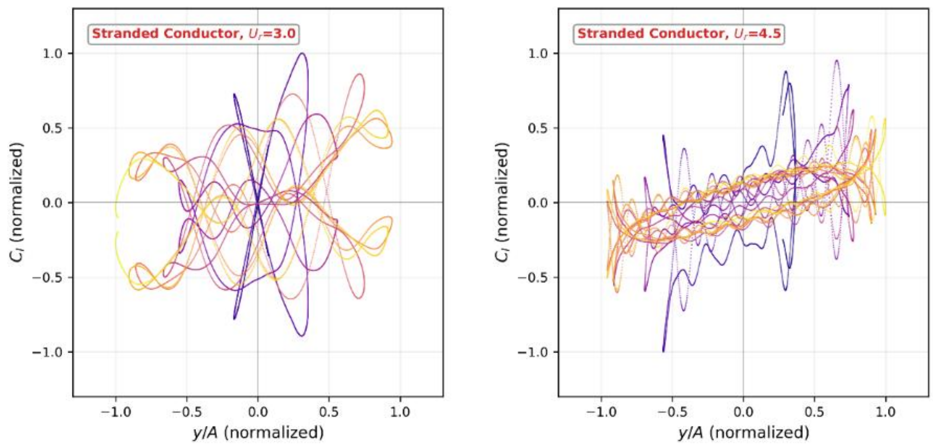


**(a)** **(b)**

**Figure 7.** *Cont.*

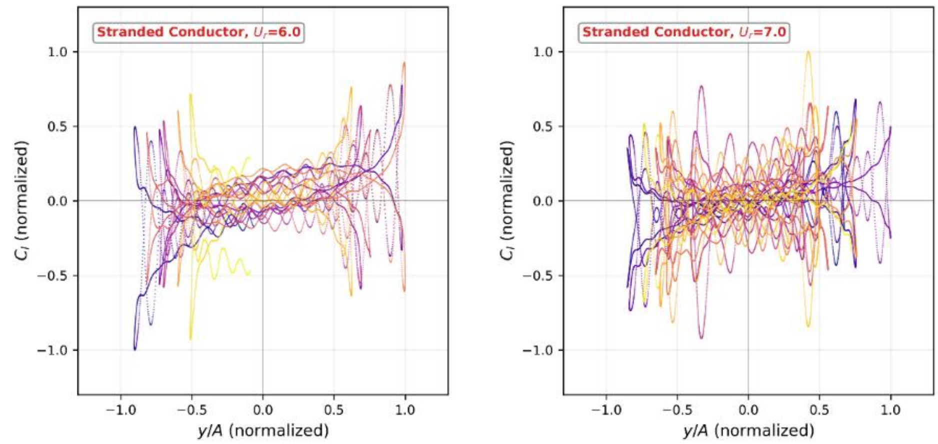


**(c)** **(d)**

**Figure 7.** Phase portraits of the resolved stranded conductor at representative reduced velocities.

At U equal to 5 m/s, equivalent to a reduced velocity of 5.0, displacement histories and lift spectra in **Figures 8** and **9** contain the same dominant low-frequency mode for both geometries, confirming that the two calculations remain locked to a common shedding tone at this velocity. Away from that peak, the stranded force spectrum shows a higher broadband floor and more energy at frequencies above the fundamental. Intermittent separation at individual outer wires is consistent with this pattern, since each wire crest can locally detach and reattach somewhat independently before merging into the primary wake. Residual noise from the direct forcing scheme occupies a similar frequency band, however, because the immersed boundary force is recomputed every step from a velocity mismatch that is never driven exactly to zero. Neither spectrum can separate the two contributions on its own, and a dedicated fixed cylinder test under the same forcing scheme would be needed to isolate the numerical component.

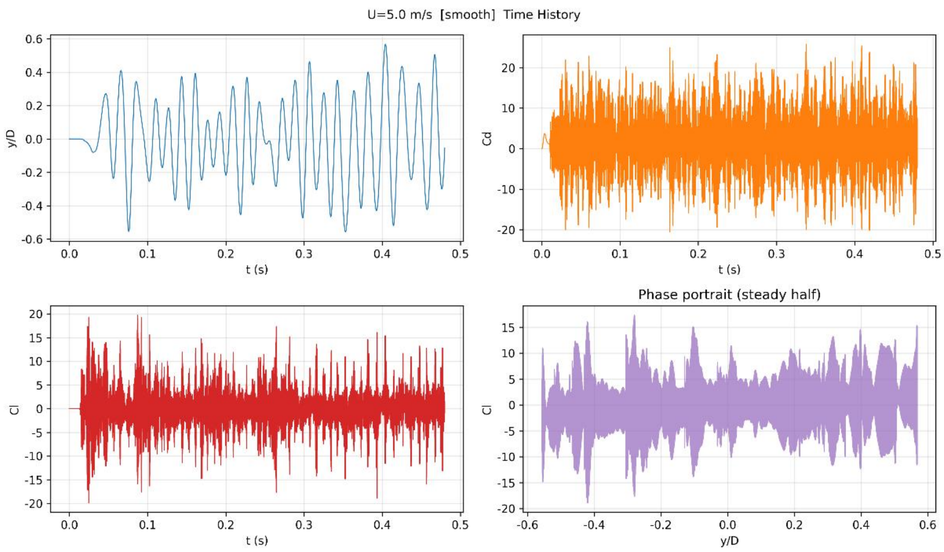


**(a)**

**Figure 8.** *Cont.*

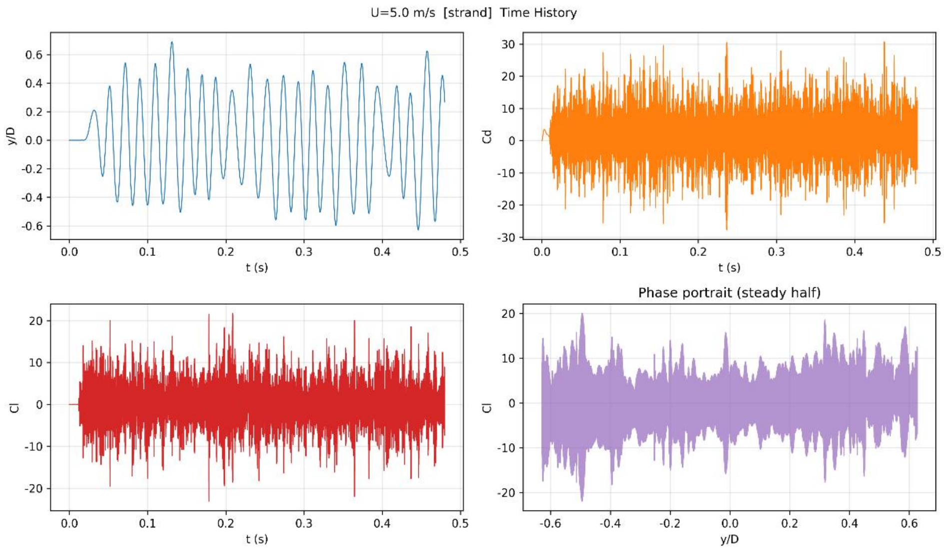


**(b)**

**Figure 8.** Representative time-history details at $U$ = 5 m/s: **(a)** Equivalent smooth cylinder; **(b)** Resolved stranded conductor.

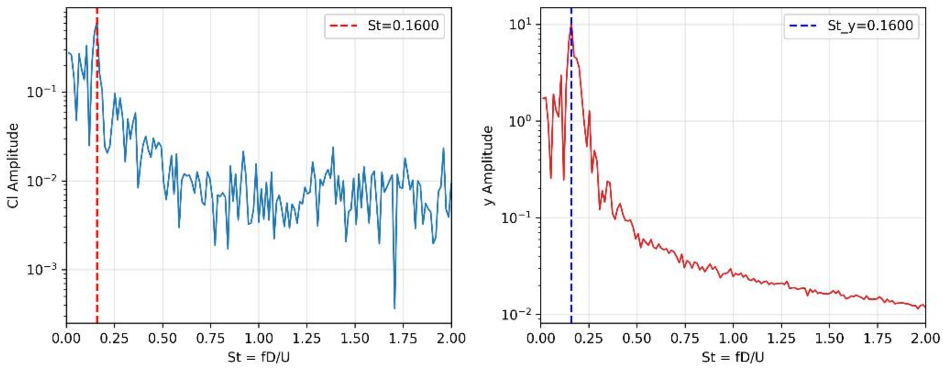


**(a)**

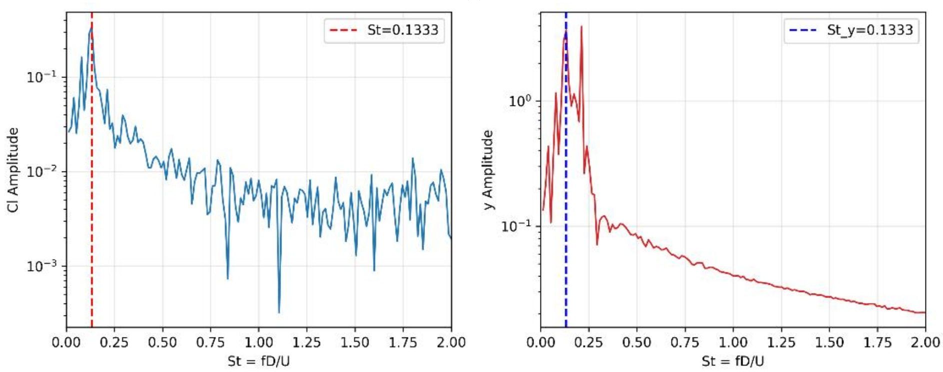


**(b)**

**Figure 9.** Frequency spectra at $U$ = 5 m/s: **(a)** Smooth-cylinder lift and displacement spectra; **(b)** Stranded-conductor lift and displacement spectra.

## 3.4. Physical wind-speed cases and displacement persistence

**Figure 10** shows the unprocessed histories at $U$ = 0.5, 1.0, 5.0 and 9.0 m/s. Phase, amplitude and slow envelope modulation all changed with speed, but the two geometries did not decay alike at 5.0 and 9.0 m/s: the cylinder trace weakened more rapidly and the stranded trace retained distinct packets. These specified-speed runs compare numerical boundaries; they are not predictions for an installed conductor.

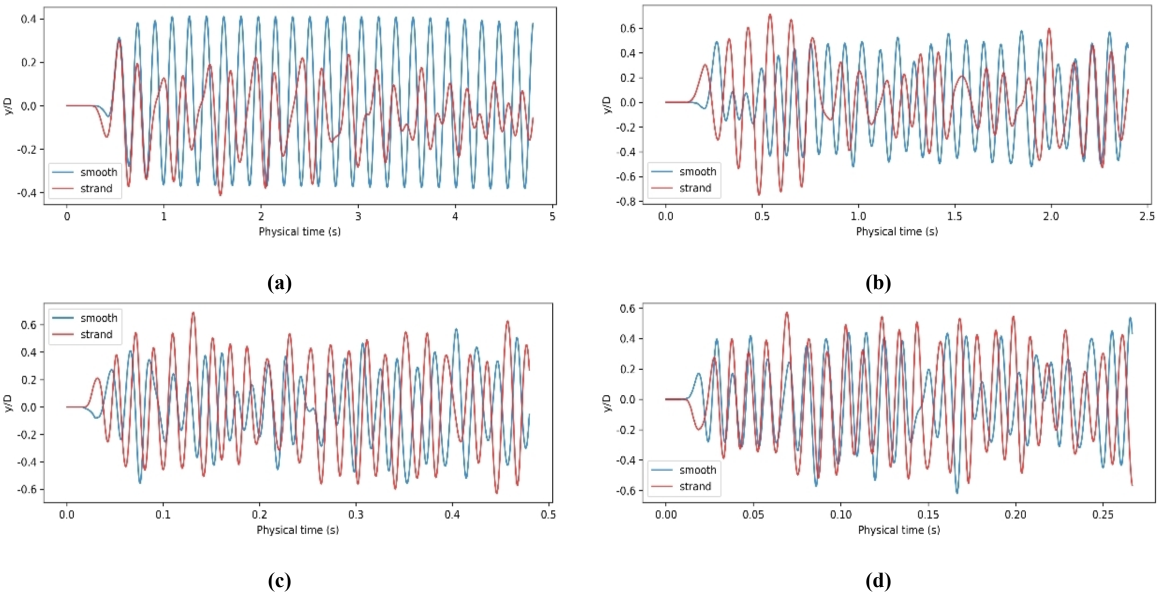


**Figure 10.** Transverse displacement histories for representative physical wind speeds: **(a)** $U$ = 0.5 m/s; **(b)** $U$ = 1.0 m/s; **(c)** $U$ = 5.0 m/s; **(d)** $U$ = 9.0 m/s.

**Figure 11** contains the time-averaged velocity fields. Differences at $U = 1$ m/s were concentrated in the two shear layers. At $U = 5$ m/s ($U_r = 5.0$), the flow accelerated around the individual outer wires and left a wider stranded wake. Since IBM force follows from velocity mismatch at each Lagrangian point, this near-wall difference can alter both integrated force and phase. The figure locates the change, but it does not isolate its contribution from the rest of the unsteady cycle.

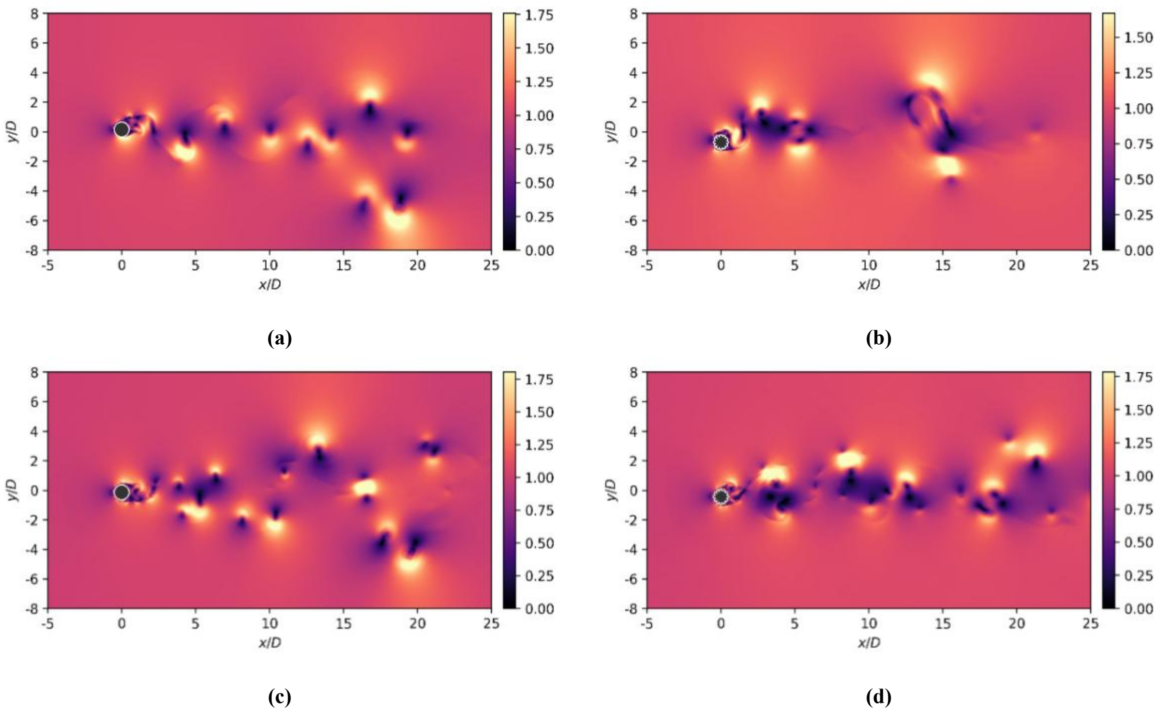


**Figure 11.** Non-dimensional velocity-magnitude fields for smooth and stranded geometries at two wind speeds: **(a)** Smooth cylinder, $U$ = 1 m/s; **(b)** Stranded conductor, $U$ = 1 m/s; **(c)** Smooth cylinder, $U$ = 5 m/s; **(d)** Stranded conductor, $U$ = 5 m/s.

**Figure 12** gives instantaneous vorticity. Behind the smooth cylinder, comparatively continuous shear layers formed an alternating Karman street. Several small cells appeared within or immediately behind strand grooves before joining the larger wake. An alternating large-scale pattern survived in both cases. Each wire crest appears to act as a small fixed promoter of separation, shedding a weak secondary vortex into the shear layer earlier than the mean separation point associated with a smooth circular profile would allow. These secondary structures do not survive individually into the far wake. They merge into the primary alternating vortices that form the wider wake pattern, but they modify the timing and strength of that primary shedding at the point where it originates. Because this modification arises at twelve fixed and evenly distributed locations around the perimeter, rather than at the two separation points of a smooth section, the resulting shear layer instability appears less sensitive to small changes in the instantaneous crossflow velocity. Such a mechanism offers a plausible explanation for why synchronization with the oscillator persists over a wider range of reduced velocity for the stranded conductor than for the smooth cylinder. Although these snapshots connect the resolved outline with a different separation pattern, frequency and phase depend on the complete unsteady cycle rather than one frame.

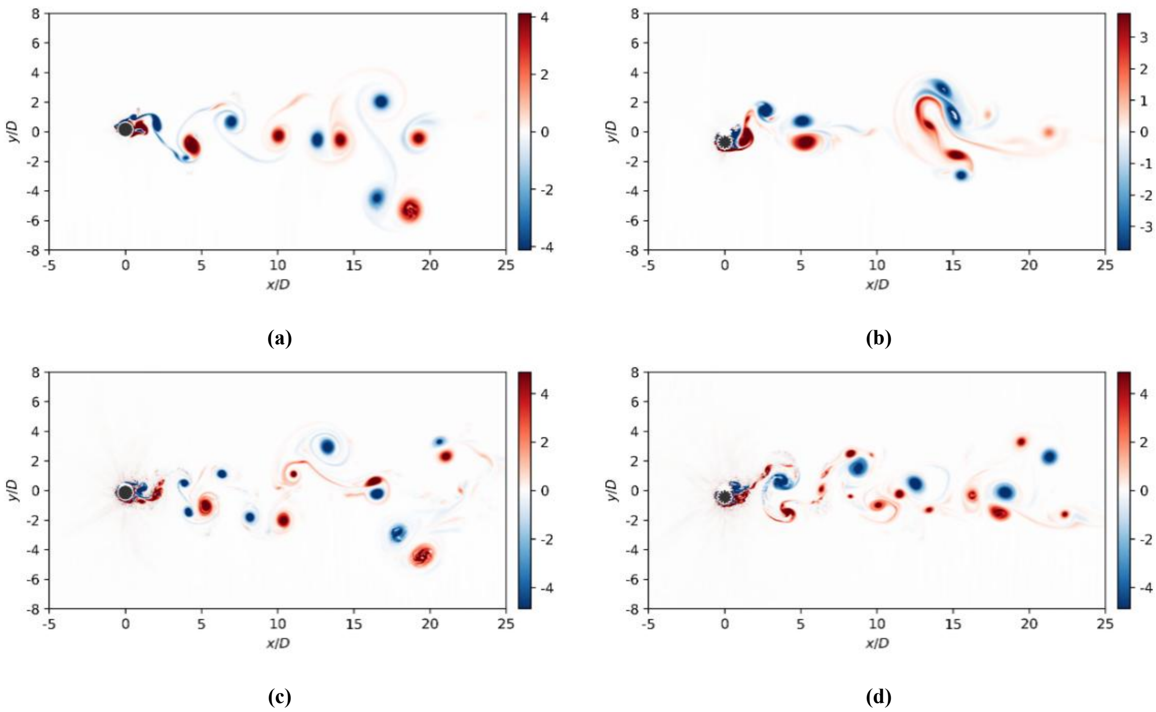


**Figure 12.** Non-dimensional vorticity fields for smooth and stranded geometries at two wind speeds: **(a)** Smooth cylinder, $U = 1$ m/s; **(b)** Stranded conductor, $U = 1$ m/s; **(c)** Smooth cylinder, $U = 5$ m/s; **(d)** Stranded conductor, $U = 5$ m/s.

At $U = 9$ m/s, corresponding to $Re = 9,600$, centreline velocity recovered earlier behind the cylinder (**Figure 13**). The stranded wake retained a larger deficit and stronger shear on either side. No turbulence model was used. **Figure 13** therefore records a persistent difference between the two numerical outlines under this setup, not a validated field-conductor wake at high Reynolds number.

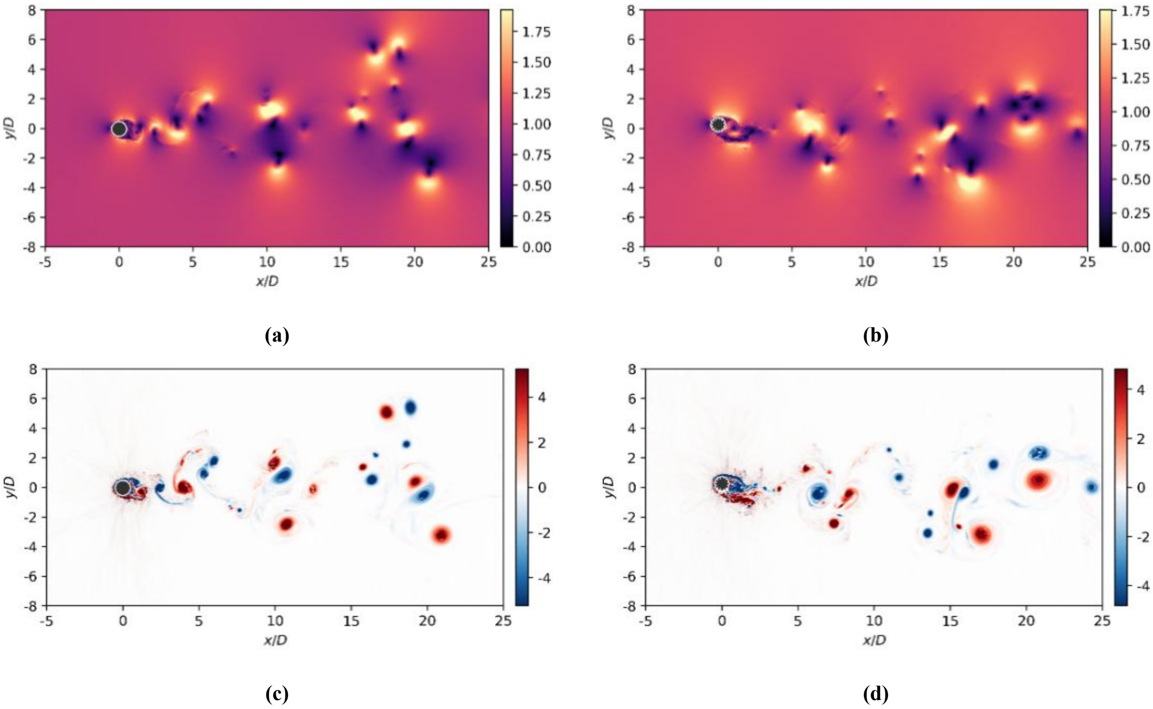


**Figure 13.** High-wind-speed flow-field comparison at $U = 9$ m/s: **(a)** Smooth-cylinder velocity magnitude; **(b)** Stranded-conductor velocity magnitude; **(c)** Smooth-cylinder non-dimensional vorticity; **(d)** Stranded-conductor non-dimensional vorticity.

At $Re = 200$, the reduced-velocity sweep is laminar and far below the operating range of roughly $10^3$ to $10^5$. Transition and background turbulence at field Reynolds numbers can weaken coherent shedding or shift the lock-in peak. Macro-roughness $d/D = 3.2/16 = 0.2$ may further change groove effects near transition and the drag crisis. One calculation was therefore added. Although **Figures 13** and **14** still show different shear layers and wake deficits, this case also lacks a turbulence model. Accordingly, the evidence is limited to geometry-dependent separation in the present two-dimensional setup; design use requires turbulent calculations, such as Large Eddy Simulation, supported by wind-tunnel measurements.

### 3.5. Wake-deficit comparison

**Figure 14** compares the centreline deficit $1 - u_x/U$. For $U = 5$ m/s ($U_r = 5.0$), the value at $x/D = 5$ was $0.479$ behind the stranded section and $0.266$ behind the cylinder. The higher-speed case, $U = 9$ m/s or $Re = 9,600$, gave values at $x/D = 10$ of $0.172$ and $0.045$. At both sampled stations the stranded wake recovered more slowly, as expected from its larger drag and sustained lift.

Bundle spacing is typically $10D$ to $20D$. At a similar downstream distance in **Figure 14**, the stranded deficit was $0.172$ at $x/D = 10$ for $U = 9$ m/s, compared with $0.045$ for the cylinder. A following sub-conductor would not see the same inflow in the two wake calculations. Only one conductor was included here, so neither wake-induced galloping nor sub-span oscillation can be inferred. Taking the deficit at ten diameters downstream for the higher tested wind speed as a reference, the stranded wake retained nearly four times the velocity deficit found behind the smooth cylinder at a distance representative of the lower end of typical bundle spacing. Even allowing for the two-dimensional and laminar limitations already noted, this comparison suggests that a smooth cylinder proxy would understate both the magnitude and the persistence of the deficit that a downstream subconductor would actually encounter if the upstream conductor's stranded surface were the governing geometry. This observation does not by itself establish a risk of wake-induced oscillation, since that outcome depends on the coupled dynamics of both conductors together. It does indicate that the smooth cylinder simplification is not a conservative one for describing the inflow seen by a following subconductor. That question requires a resolved two-conductor or complete bundle model.

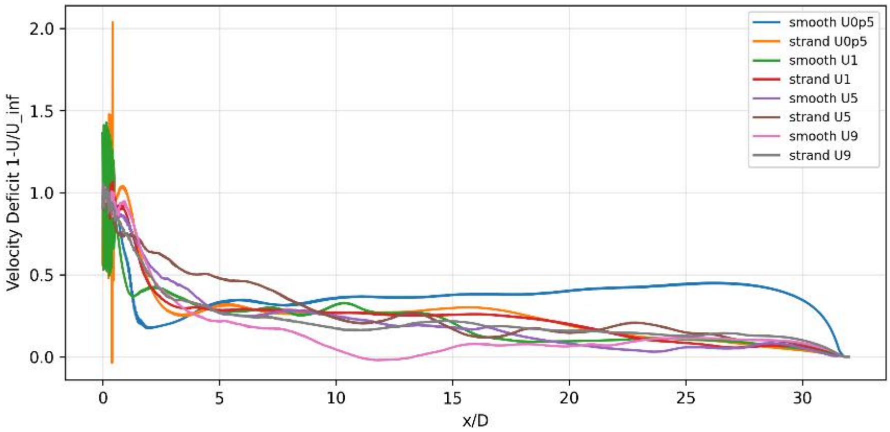


**Figure 14.** Centreline velocity-deficit recovery behind the smooth and stranded geometries for representative physical wind speeds.

## 4. Conclusion

The fixed-grid calculations differ in one prescribed boundary. One is the resolved JL/G1A-95/55 strand envelope and the other is a circle with the same diameter; the Cartesian lattice, flow algorithm and transverse oscillator are shared. Differences between the paired runs can therefore be traced to the two-dimensional outline without a concurrent change in body-fitted mesh.

With the selected Reynolds number and oscillator, the stranded response extended over a wider branch. Cylinder amplitude reached $A_{y,max}/D = 0.443$ at $U_r = 4.0$ but had fallen to $0.188$ by $U_r = 9.0$; the stranded values were $0.517$ at $U_r = 7.0$ and $0.472$ at $U_r = 9.0$. Mean drag over the sweep was $16.7\%$ higher for the stranded section, and its aerodynamic power remained positive at the upper limit ($C_P > 0$). Phase, vorticity and wake-deficit records associate the difference with separation at the grooves and a later change in lift relative to velocity, an interpretation confined to these two-dimensional calculations.

Several steps remain before the result can be transferred to an operating span. Straight two-dimensional grooves omit spanwise flow caused by the helical lay; the benchmark values $m^* = 2.0$ and $\zeta = 0.01$ also give much less mass damping than a conductor in air, and the $Re = 200$ sweep is laminar. A useful next test is a three-dimensional helical section at a field Reynolds number, followed by wind-tunnel measurements of force, phase and displacement. Until such comparisons are available, the response branches reported here should not replace smooth-cylinder relations in span-level design.

**Author contributions:** Conceptualization, XL and YL; methodology, XL and MN; software, XL; validation, XL, MN, GW, ZY and YZ; formal analysis, XL and YZ; investigation, XL and MN; resources, YZ; data curation, XL; writing—original draft preparation, XL; writing—review and editing, MN, GW and YZ; visualization, XL and GW; supervision, YL; project administration, YL; funding acquisition, YL. All authors have read and agreed to the published version of the manuscript.

**Funding:** This research was funded by the Science and Technology Project of China Southern Power Grid Co., Ltd. (Grant No. GDKJXM20240295).

**Institutional review board statement:** Not applicable.

**Informed consent statement:** Not applicable.

**Data availability statement:** The data supporting this study's findings are available from the corresponding author upon reasonable request. The numerical scripts, processed summary tables and generated figures used to prepare this manuscript are retained in the project workspace.

**Acknowledgment:** The authors acknowledge the support of Guangdong Power Grid Co., Ltd. for the conductor vibration research programme.

**Conflict of interest:** The authors declare no conflict of interest.

**AI use statement:** During the preparation of this work, the authors used Grammarly and Claude for grammar and sentence check. The authors subsequently reviewed and edited the content as necessary and take full responsibility for the final content of the published article.

## References

1. International Electrotechnical Commission. Overhead Lines—Requirements and Tests for Aeolian Vibration Dampers. IEC 61897:2020. International Electrotechnical Commission; 2020.
2. Liu J, Yan B, Mou Z, et al. Numerical study of aeolian vibration characteristics and fatigue life estimation of transmission conductors. PLOS ONE. 2022; 17(1): e0263163. doi: 10.1371/journal.pone.0263163
3. Yang S, Chouinard L, Langlois S, et al. Evaluation of fatigue damage for undamped overhead conductors under aeolian vibration. IEEE Transactions on Power Delivery. 2025; 40(3): 1647–1655. doi: 10.1109/TPWRD.2025.3558649
4. Babaei M, Asemi K. Stress analysis of functionally graded saturated porous rotating thick truncated cone. Mechanics Based Design of Structures and Machines. 2022; 50(5): 1537–1564. doi: 10.1080/15397734.2020.1753536
5. Kiarasi F, Babaei M, Asemi K, et al. Free vibration analysis of thick annular functionally graded plate integrated with piezo-magneto-electro-elastic layers in a hygrothermal environment. Applied Sciences. 2022; 12(20): 10682. doi: 10.3390/app122010682
6. Nazari H, Babaei M, Kiarasi F, et al. Geometrically nonlinear dynamic analysis of functionally graded material plate excited by a moving load applying first-order shear deformation theory via generalized differential quadrature method. SN Applied Sciences. 2021; 3(11): 847. doi: 10.1007/s42452-021-04825-9
7. Zhou Y, Zhang Y, Chirukam BN, et al. Free vibration analyses of stiffened functionally graded graphene-reinforced composite multilayer cylindrical panel. Mathematics. 2023; 11(17): 3662. doi: 10.3390/math11173662
8. Shen X, Li T, Xu L, et al. Free vibration analysis of FG porous spherical cap reinforced by graphene platelet resting on Winkler foundation. Advances in Nano Research. 2024; 16(1): 11–26. doi: 10.12989/anr.2024.16.1.011

9. Chan J, Havard D, Rawlins C, et al. EPRI Transmission Line Reference Book: Wind-Induced Conductor Motion, 2nd ed. Electric Power Research Institute; 2009. Available online: https://hdl.handle.net/2268/102166
10. Diana G. Modelling of Vibrations of Overhead Line Conductors: Assessment of the Technology. CIGRE Green Books; 2018.
11. Diana G, Cigada A, Belloli M, et al. Stockbridge-type damper effectiveness evaluation. I. Comparison between tests on span and on the shaker. IEEE Transactions on Power Delivery. 2003; 18(4): 1462–1469. doi: 10.1109/TPWRD.2003.817797
12. CIGRE. Overhead Conductor Safe Design Tension with Respect to Aeolian Vibrations. CIGRE; 2005.
13. Zhong B, Cai M, Hu M, et al. Enhancing iced 8-bundled conductor galloping prediction for UHV transmission line infrastructure through high-fidelity aerodynamic modeling. Infrastructures. 2025; 10(8): 201. doi: 10.3390/infrastructures10080201
14. Krüger T, Kusumaatmaja H, Kuzmin A, et al. The Lattice Boltzmann Method: Principles and Practice. Springer; 2017. doi: 10.1007/978-3-319-44649-3
15. Latt J, Malaspinas O, Kontaxakis D, et al. Palabos: Parallel lattice Boltzmann solver. Computers & Mathematics with Applications. 2021; 81: 334–350. doi: 10.1016/j.camwa.2020.03.022
16. Krause MJ, Kummerländer A, Avis SJ, et al. OpenLB—Open source lattice Boltzmann code. Computers & Mathematics with Applications. 2021; 81: 258–288. doi: 10.1016/j.camwa.2020.04.033
17. Ataei M, Salehipour H. XLB: A differentiable massively parallel lattice Boltzmann library in Python. Computer Physics Communications. 2024; 300: 109187. doi: 10.1016/j.cpc.2024.109187
18. Hou G, Wang J, Layton A. Numerical methods for fluid–structure interaction: A review. Communications in Computational Physics. 2012; 12(2): 337–377. doi: 10.4208/cicp.291210.290411s
19. Sotiropoulos F, Yang X. Immersed boundary methods for simulating fluid–structure interaction. Progress in Aerospace Sciences. 2014; 65: 1–21. doi: 10.1016/j.paerosci.2013.09.003
20. Kim W, Choi H. Immersed boundary methods for fluid–structure interaction: A review. International Journal of Heat and Fluid Flow. 2019; 75: 301–309. doi: 10.1016/j.ijheatfluidflow.2019.01.010
21. Li Z, Cao W, Le Touzé D. On the coupling of a direct-forcing immersed boundary method and the regularized lattice Boltzmann method for fluid–structure interaction. Computers & Fluids. 2019; 190: 470–484. doi: 10.1016/j.compfluid.2019.06.030
22. Griffith BE, Patankar NA. Immersed methods for fluid–structure interaction. Annual Review of Fluid Mechanics. 2020; 52: 421–448. doi: 10.1146/annurev-fluid-010719-060228
23. Wang L, Liu Z, Rajamuni M. Recent progress of lattice Boltzmann method and its applications in fluid–structure interaction. Proceedings of the Institution of Mechanical Engineers, Part C: Journal of Mechanical Engineering Science. 2023; 237(11): 2461–2484. doi: 10.1177/09544062221077583
24. Wu X, Chen F, Zhou S. Stationary and flow-induced vibration of two elliptic cylinders in tandem by immersed boundary-MRT lattice Boltzmann flux solver. Journal of Fluids and Structures. 2019; 91: 102762. doi: 10.1016/j.jfluidstructs.2019.102762
25. Yan H, Zhang G, Wang S, et al. Simulation of vortex shedding around cylinders by immersed boundary-lattice Boltzmann flux solver. Applied Ocean Research. 2021; 114: 102763. doi: 10.1016/j.apor.2021.102763
26. Jiao H. Vortex-Induced Vibration of Circular Cylinders Using Multi-Block Immersed Boundary-Lattice Boltzmann Method [PhD Thesis]. University College London; 2021.
27. Xu P, Zhou Q, Luo Z, et al. An efficient numerical framework for fluid–structure interaction based on the LBM-IBM method and its applications. Acta Aerodynamica Sinica. 2026; 44(3): 132–144. doi: 10.7638/kqdlxxb-2025.0245 (in Chinese)
28. Zhao M, Cheng L, An H, et al. Three-dimensional numerical simulation of vortex-induced vibration of an elastically mounted rigid circular cylinder in steady current. Journal of Fluids and Structures. 2014; 50: 292–311. doi: 10.1016/j.jfluidstructs.2014.05.016
29. Bao Y, Huang C, Zhou D, et al. Two-degree-of-freedom flow-induced vibrations on isolated and tandem cylinders with varying natural frequency ratios. Journal of Fluids and Structures. 2012; 35: 50–75. doi: 10.1016/j.jfluidstructs.2012.08.002
30. Martini S, Morgut M, Pigazzini R. Numerical VIV analysis of a single elastically mounted cylinder: Comparison between 2D and 3D URANS simulations. Journal of Fluids and Structures. 2021; 104: 103303. doi: 10.1016/j.jfluidstructs.2021.103303
31. Wang Z, Fan D, Triantafyllou MS. Illuminating the complex role of the added mass during vortex-induced vibration.

Physics of Fluids. 2021; 33(8): 085120. doi: 10.1063/5.0059013
32. Raza SA, Irawan YH, Chern MJ. Effect of grid size and initial conditions on vortex-induced vibration of a circular cylinder. Ocean Engineering. 2022; 263: 112332. doi: 10.1016/j.oceaneng.2022.112332
33. Jia L, Sang S, Shi X, et al. Investigation on numerical simulation of VIV of deep-sea flexible risers. Applied Sciences. 2023; 13(14): 8096. doi: 10.3390/app13148096
34. Jiang H, Ju X, Zhao M, et al. Large-eddy simulation of vortex-induced vibration of a circular cylinder at Reynolds number 10 000. Physics of Fluids. 2024; 36(8): 085113. doi: 10.1063/5.0219933
35. Wang L, Liu Z, Jin BR, et al. Wall-modeled large eddy simulation in the immersed boundary-lattice Boltzmann method. Physics of Fluids. 2024; 36(3): 035167. doi: 10.1063/5.0198252
36. Yu Z, Wang E, Bao Y, et al. VIV of two rigidly coupled side-by-side cylinders at subcritical Re. International Journal of Mechanical Sciences. 2024; 267: 108961. doi: 10.1016/j.ijmecsci.2024.108961
37. Williamson CHK, Govardhan R. A brief review of recent results in vortex-induced vibrations. Journal of Wind Engineering and Industrial Aerodynamics. 2008; 96(6–7): 713–735. doi: 10.1016/j.jweia.2007.06.019
38. Williamson CHK, Brown GL. A series in 1/√Re to represent the Strouhal–Reynolds number relationship of the cylinder wake. Journal of Fluids and Structures. 1998; 12: 1073–1085. doi: 10.1006/jfls.1998.0184
39. White FM. Fluid Mechanics, 6th ed. McGraw-Hill; 2006.